OPEN ACCESS
IOP Publishing
Measurement Science and Technology
Meas. Sci. Technol. **35** (2024) 015207 (12pp)
https://doi.org/10.1088/1361-6501/ad044f

Development of time-resolved photoluminescence microscopy of semiconductor materials and devices using a compressed sensing approach

Aidas Baltušis[1,2,3,*], **George Koutsourakis**[1,*], **Sebastian Wood**[1] and **Stephen J Sweeney**[2,3]

[1] National Physical Laboratory, Hampton Road, Teddington, Middlesex TW11 0LW, United Kingdom
[2] Advanced Technology Institute and Department of Physics, University of Surrey, Guildford GU2 7XH, United Kingdom
[3] James Watt School of Engineering, College of Science and Engineering, University of Glasgow, Glasgow G12 8LT, United Kingdom

E-mail: 2836714B@student.gla.ac.uk and george.koutsourakis@npl.co.uk

Received 4 May 2023, revised 21 September 2023
Accepted for publication 17 October 2023
Published 26 October 2023

Abstract

Charge carrier lifetime is a key property of semiconductor materials for photonic applications. One of the most established methods for measuring lifetimes is time-resolved photoluminescence (TRPL), which is typically performed as a single-point measurement. In this paper, we demonstrate a new time-correlated single photon counting method (TCSPC) for TRPL microscopy, for which spatial information can be achieved without requiring point-by-point scanning through the use of a compressed sensing (CS) approach. This enables image acquisition with a single pixel detector for mapping the lifetime of semiconductors with high repeatability. The methodology for signal acquisition and image reconstruction was developed and tested through simulations. Effects of noise levels on the reliability and quality of image reconstruction were investigated. Finally, the method was implemented experimentally to demonstrate a proof-of-concept CS TCSPC imaging system for acquiring TRPL maps of semiconductor materials and devices. TRPL imaging results of a semiconductor device acquired using a CS approach are presented and compared with results of TRPL mapping of the same excitation area measured through a point-by-point method. The feasibility of the methodology is demonstrated, the benefits and challenges of the experimental prototype system are presented and discussed.

Supplementary material for this article is available online

Keywords: compressed sensing (CS), semiconductor characterisation, time-resolved photoluminescence (TRPL), charge carrier lifetimes, signal processing, recombination

* Authors to whom any correspondence should be addressed.

1. Introduction

Spatial variations of charge carrier lifetimes within compound semiconductor materials and devices are of key interest for both research and industrial applications. Spatial inhomogeneity and defects can have significant impact on device yields and operation. Understanding such variations is important for a range of device types and sizes, from $\sim\mu m^2$ scale vertical cavity surface emitting lasers and photodetectors, through to large area wafers (cm^2) for power electronic applications or solar cells. Fast, accurate and repeatable measurement techniques for quality assurance at different stages of device fabrication can lead to a reduction in both production costs and material waste. The accurate measurement of material and device spatial quality and characterisation of defects is also required for identifying failure mechanisms related to specific defects [1, 2].

Charge carrier lifetime is commonly used as one of the parameters that describes material quality and determines the overall efficiency of devices [3–5]. The parameter is used in characterisation for various devices, such as photovoltaics (PV) [6], laser diodes [7], light-emitting diodes [8] and other semiconductor devices. One of the most established techniques for measuring charge carrier lifetimes is time-resolved photoluminescence (TRPL). The sample is excited using a laser pulse, resulting in photoluminescence (PL) emission. The PL signal is detected with high temporal resolution (down to $\sim$1 ps), allowing determination of the decay time of the signal and the associated charge carrier lifetimes. In this work, we use the time-correlated single-photon counting (TCSPC) [9] approach for acquiring TRPL measurements. The TRPL signals in semiconductors considered here are on the order of ns, however, they can cover a broad range of lifetimes, ranging from sub-ns to ms depending on the material. In this work, a photomultiplier tube (PMT) is used to perform TCSPC. A feature of TCSPC is that signal acquisition is spread over many measurement cycles, improving temporal resolution and signal strength.

The PL lifetimes provide insights regarding the radiative and non-radiative recombination processes happening within the material [10–12]. As the material returns towards its equilibrium state, excited carriers recombine through different routes—radiatively or non-radiatively through Shockley–Reed–Hall or Auger recombination. Each of these processes occurs on different timescales and, therefore, corresponds to different carrier lifetimes [13, 14].

Acquiring spatially-resolved measurements reveals the variations in charge carrier lifetimes across the measured sample, which is useful in terms of understanding the quality of the material [8]. Having the spatial information helps understand the charge carrier diffusion within the material and identify recombination centres [6]. Typically, this is achieved by either raster scanning the sample or rotating the sample and moving the point radially. However, there are disadvantages with this type of approach. The mechanical movement can compromise the spatial resolution and repeatability of the measurements. Also, these types of measurements can take a relatively long time to acquire, due to the need to measure the PL decay at every point individually to get an accurate charge carrier lifetime image.

Regardless of the measurement approach, the final result of TRPL mapping is a compressible natural image—most natural signals and images will have a concise representation if expressed in a convenient basis [15]. Such images measured with raster techniques can be accurately compressed for storage using less data than the originally acquired dataset [16], this suggests the potential to apply the compressed sensing (CS) paradigm to TRPL mapping.

CS theory was introduced in the early 2000s by Donoho [17], and Candes and Tao [18]. It provides a methodology for acquiring a compressed signal directly through specially designed measurements. For the CS theory to be applicable, two conditions must be met: (1) the signal must be sparse and (2) the measurement functions used must be designed such that they are incoherent with the signal in its natural or transformed basis [19, 20]. Details on how these conditions were met in this work are given in section 2. After acquiring the compressed measurements, the original signal can be reconstructed by solving an optimisation problem for the sparsest solution consistent with the measurements. For imaging applications, this means a single pixel detector can be used to acquire a high-resolution image, provided that the spatial information is encoded into the measurement itself [21]. In practice, spatial information can be encoded into the measurement with digital light processing (DLP), using a digital micromirror device (DMD) [22]. The DMD allows the necessary measurement functions i.e. spatial patterns to be projected onto the sample or detector so that the compressed measurement can be acquired. CS and DLP have been successfully applied in various measurement applications such as light-beam induced current imaging for PV [23] and fluorescence microscopy for biology applications [24]. Recent work has also been carried out towards achieving temporally or spectrally resolved PL imaging using liquid crystal spatial modulators [25]. There have also been recent publications of implementing CS for hyperspectral imaging by utilising a DMD on the detection side of the optical system [26]. Application of CS in measurement systems is also possible without using a DMD, in techniques where its integration is difficult or impossible and CS is used to speed up measurements [27].

In this work, we demonstrate how CS can be adopted for TRPL single pixel imaging. We have evaluated a new CS TRPL mapping approach, based on a DMD-based, TCSPC technique which can achieve high spatial and temporal resolutions. The methodology of CS TRPL was developed through simulation work and implemented in a prototype experimental setup. A major challenge in implementing CS theory for measuring charge carrier lifetimes comes from it being a derived measurement; the carrier lifetime cannot be measured directly and must be determined by fitting an appropriate function to the measured TRPL signal decay. A dedicated computational model was developed for simulating raster and CS TRPL imaging of samples with non-uniform carrier lifetimes. To process these measurements, a reconstruction technique was developed, capable of recovering charge carrier lifetime maps from CS TRPL measurements. The methodology

was validated through simulations, where under-sampling and noise limits for this application were investigated. An initial experimental approach is presented, with results demonstrating the challenges and features of this method. The results indicate the route towards a new TRPL mapping methodology, that can potentially offer higher repeatability, spatial accuracy and measurement speed compared to scanning approaches.

2. Methods

2.1. Principle of CS imaging

A TRPL mapping system would traditionally use a point-by-point scanning approach. In CS TRPL, the aim is to simultaneously sample the whole area of interest, eliminating the need for translational movements. To achieve this, predefined patterns are projected onto the area of interest, using a spatial encoder, measuring the PL decay for each of the patterns with the TCSPC system. The resolution of the projected patterns is equivalent to the required resolution of the final reconstructed images. The series of patterns are projected, acquiring for each pattern the combined TRPL response for the sum of all illuminated pixels. The final reconstruction then calculates the TRPL response of each pixel, eventually building a TRPL map.

One of the benefits of CS theory is that it allows a method for inferring the response or signal of each individual pixel, even when not independently measuring it. Instead, the response of each pixel can be acquired from combined measurements of known patterns. The reconstruction works by taking advantage of the sparsity of natural signals—a constraint is added, only allowing solutions with a small number of non-zero coefficients in some transform domain. A detailed explanation of CS methodology and applying it for single-pixel cameras is described in work by Duarte *et al* [21]. A more detailed description of the reconstruction is also given in section 2.2.5.

The other advantage of CS approach is under-sampling. In a typical point-by-point measurement, each point of the image must be measured. If a pixel is missed there is no information acquired about it. This means that the display resolution of any image is equivalent to the number of measurements taken. However, by using a CS approach, the number of measurements can be significantly reduced. The theoretical minimum number of measurements (r) is approximately given by equation (1) [28],

$$r \approx k_1 K log\left(\frac{q}{K}\right). \tag{1}$$

where K is the number of significant elements of the image when compressed in a sparse basis, q is the number of pixels in the image and therefore q/K is analogous to a compression ratio. k_1 is a constant multiplier, relating to the quality of the measurements [29]. If the measurements are perfectly incoherent with the sparsifying basis (e.g. discrete cosine transform (DCT)), then $k_1 = 1$. In practice, it is beneficial to sample more than r measurements to ensure accurate reconstruction.

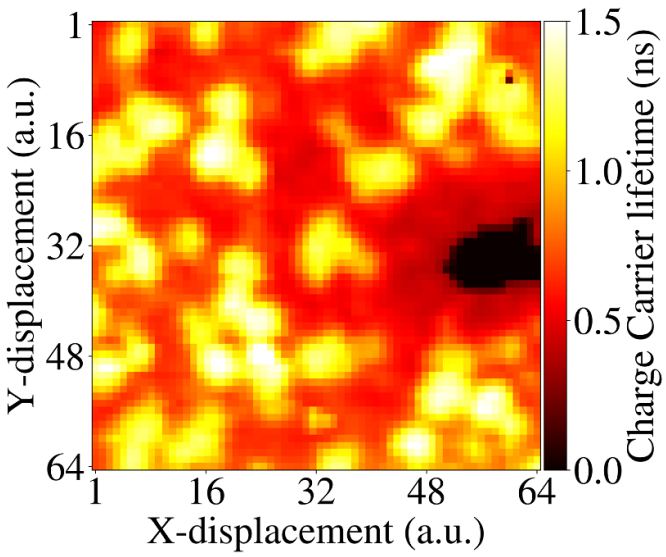

Figure 1. A carrier lifetime image of a PV device, which was used to generate a 'virtual' sample for simulating TRPL measurements.

Due to under-sampling, the solution becomes an underdetermined linear system—there are more unknowns than measurements, which has either infinite solutions or none. From these possible solutions, a reconstruction algorithm selects the most likely by maximising sparsity in the transform domain. Finally, work done by Candes [19] showed that ℓ_1 norm minimisation (also known as least residual norm or taxicab norm) solutions have a high probability of correctly counting and finding the non-zero solutions. Efficient ℓ_1 norm algorithms pre-date the concept of CS [30].

2.2. CS TRPL simulations

A simple model was built to run simulations to study the behaviour of the whole spatial imaging system when applying CS TRPL. The simulations were performed using Python 3.8 [31] making use of the available open-source libraries within SciPy ecosystem [32], Matplotlib [33] and Numba [34].

2.2.1. Defining a virtual sample. The goal of the simulation process was to investigate the feasibility of applying CS to TRPL imaging and determine the correct process for reconstructing lifetime maps.

For the simulation purposes, a charge carrier lifetime map of an area of cadmium indium gallium selenide (CIGS) PV device was used, as shown in figure 1. In principle, any image or test structure could have been used for this. However, this image was chosen to be representative of what might be expected in a physical CS TRPL measurement. From theory [35], the charge carrier lifetime is expected to follow an exponential decay function, shown in equation (2),

$$I(t) = \sum_{i}^{k} A_i \exp\left(-\frac{t}{\tau_i}\right). \tag{2}$$

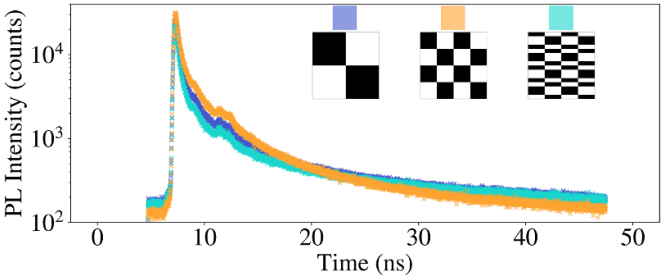

Figure 2. Illustration of a typical CS TRPL measurement. The insets show examples of some of the Hadamard patterns used in the measurement acquisition. Every pattern covers the same overall area on the sample but varying points within that area are being excited. The different TRPL signals displayed in the figure serve as examples of the differences between measurements of the different patterns. By running these data through a reconstruction algorithm, the spatial variations across the imaged area are calculated.

where $I(t)$ is the TRPL signal of the sample at time t, k is number of recombination paths present, A_i is the amplitude and τ_i is the charge carrier lifetime, for recombination route i. In the simplest case, $k = 1$ where there is only one type of recombination present, which was used in this work for simplicity of the calculations. When $k > 1$, the simulation process will stay the same and only the shape of the TRPL decay curve will change. Therefore, by defining a map of charge carrier lifetime values, we can calculate the TRPL of each pixel of the virtual sample. The aim of our simulation process is to simulate TCSPC measurements using compressive sampling and reconstruct the initial lifetime map, shown in figure 1.

2.2.2. Generating patterns. To simulate the CS process, suitable binary projection patterns must be generated. The spatial resolution of the patterns used dictates the spatial resolution of the reconstructed image, i.e. if we use 64×64 resolution patterns, then the final reconstructed images will also have the same resolution.

Two types of patterns were considered in these simulations—one based on pseudo-random number generation and the other on a Walsh–Hadamard transform (WHT) [23]. Examples of a few Hadamard patterns are shown in figure 2. Both have their advantages and disadvantages. The random sampling patterns benefit from minimal coherence with transfer domains [36]. Random patterns must be stored in memory for reconstruction to work. The amount of memory required scales with the square of the pattern resolution. To store all the random patterns needed for measuring a 10^6 pixel image, a matrix with 10^{12} entries would have to be stored in memory. Therefore, using random patterns quickly becomes impractical if high resolution images are desired. In this work, measurements based on WHT patterns were used. These patterns have been shown to satisfy the incoherence requirement needed for CS theory to be applicable in transform domains such as DCT or discrete wavelet transform (DWT) [37, 38]. Any small amount of coherence that might be present between these patterns and the measured signal can be accounted for by increasing the number of total measurements needed, as shown in equation (1).

The biggest advantage of using Hadamard patterns is the reduced computational complexity when generating them. Efficient algorithms have been written to generate such patterns repeatedly and quickly. Furthermore, these can be described as a transform acting on the measurement. The patterns do not need to be stored in memory for reconstruction, instead a linear operator based on WHT can be used which allows high resolution images without requiring an unreasonable amount of computer memory. This is similar to the way more common transforms are used, *e.g.* algorithms have been created to compute Fast Fourier Transform quickly, without needing to first calculate the whole transform matrix. Hadamard patterns have been already demonstrated for sampling in recent CS imaging applications [23].

2.2.3. Simulating TCSPC sampling. We used a simple statistical model for simulating TCSPC emission for both single point and CS simulations. The TCSPC principle works by extending the TRPL collection over many laser pulses, enabling very weak PL signals to be acquired [39]. This is possible as long as the arrival of each detected photon can be precisely timed and the TRPL response of the sample does not change throughout the measurement cycle.

There are three parameters used to statistically simulate TCSPC—lifetime τ_i of the measured pixel, probability p of an excitation pulse resulting in a detectable photon, and the number of laser pulses. This probability must be kept suitably low, typically below 0.02 to prevent photon pile-up effects [40]. The probability distribution for the number of photons per pulse is a Poisson distribution with the mean number of photons per pulse converging to p for $p \ll 1$. For each pulse, the number of photons reaching the detector is sampled from the Poisson distribution. If no photons are detected, the algorithm moves on to the next pulse and performs the check again. When a photon is detected, a photon arrival time is sampled from an exponential distribution. Due to stochastic nature of PL emission, multiple photons might arrive at the detector between the laser pulses. However, the detectors used in TCSPC setups are only capable of recording a single photon after a laser pulse. Therefore, if multiple photons reach the detector, only the first one would be recorded. To simulate this, when multiple photons are detected, the arrival time of each of them is determined. The arrival times are compared, and the time of the fastest photon is recorded. The photon arrival time gets placed into a histogram, where the width of each bin of the histogram represents the temporal resolution of the measurement. By repeating this process over a fixed number of laser pulses, the histogram gets populated. After a large number of pulses, typically $10^7 - 10^8$, the histogram becomes equivalent to the TRPL response of the measured area. These assumptions work in the limit that the pixel size is large compared to the diffusion length, and therefore that measured emission lifetime is not influenced by the lifetimes of nearby pixels.

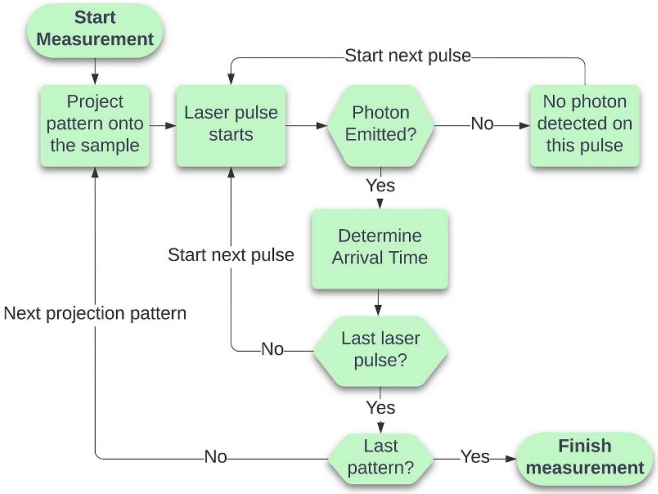

Figure 3. Flowchart of CS TRPL measurement process. After projecting a given pattern, a TCSPC method is used to acquire TRPL response of the whole area excited by the projected pattern. Each pattern is measured for a fixed measurement duration, determined by the number of laser pulses applied.

2.2.4. Simulating sampling with a DMD. A specific challenge for this work is that, unlike other implementations of CS imaging in literature in which the measurement result of each pattern is a single value, each projected pattern results in a decay curve, which is the TRPL signal. A few typical raw measurements from CS TRPL are shown in figure 2.

To simulate the excitation with different illuminated patterns projected on the sample instead of just a point excitation, each generated pattern is used to mask the virtual sample. The measurement acquisition can be written down as $b = Cx$, where b is a vector containing all the measured values, C contains all the projected patterns and x is the sample being measured. The TCSPC simulation algorithm described above is applied to the masked sample. In other words, the PL emission is only possible from the parts of the sample which are virtually excited by the given pattern. A flowchart of the measurement process is shown in figure 3.

The method is repeated for several patterns, determined by the desired sampling level, up to a maximum number of patterns to the target image display resolution. As highlighted in the earlier section, under-sampling is one of the key advantages of CS. Fewer measurements than pixels in the final image are sufficient for a meaningful reconstructed image.

Once the Monte–Carlo simulation is complete, the results file is a matrix, as indicated in table 1. Each row corresponds to a different pattern that was applied during the measurement and each column to a number of photon arrival events for that particular time bin. These data are then used to reconstruct a TRPL data cube which consists of the TRPL maps for all these bins.

2.2.5. Reconstruction algorithm. To reconstruct the acquired measurements into an image, a convex optimization problem must be solved.

A free-source package SPGL1 [41–43] is used precisely for this purpose. The package is a solver for large-scale ℓ_1 norm regularized least squares and is designed to solve three problems—Basis Pursuit (BP), Basis Pursuit Denoise and Lasso. The results from both the simulation and prototype system are a matrix B, as illustrated in table 1. However, the reconstruction algorithms can only accept 1D data which would work if for every pattern there was only one signal value, instead of a decay curve. Our chosen approach is splitting the measurement matrix into independent measurement vectors b_g for each time bin. To promote the sparsity of the signal, it is useful to express the original image x in a transform domain, such that $s_g = \Psi x_g$. The measurement process of each bin is then described by equation (3),

$$b_g = C\Psi^{-1}s_g \tag{3}$$

where C is a column vector form of the projected pattern, Ψ is the transform matrix of a chosen sparsifying basis such as DCT or DWT and s_g are the image's coefficients of the sample in a column vector form for the corresponding bin number. The reconstruction is carried out for each bin independently of each other, solving the equation (4)

$$\widehat{s_g} = \underset{s_g}{\operatorname{argmin}} ||s_g||_1$$

$$\text{subject to } b_g = C\Psi^{-1}s_g \tag{4}$$

where $\|\cdot\|_1$ is the ℓ_1 norm. The result of the optimization is a vector of length n for each bin of the reconstruction. Each of the vector values correspond to the sparsest solution of PL intensity information at a specific time slice in the chosen transform domain (DCT in this case). By applying the inverse of the transform to each of these vectors, the coefficients are converted to histograms for each pixel. After repeating the reconstruction process for every bin in the measurement file, the final result is a matrix of the format shown in table 2. This can be simply reshaped into a 3D data cube, representing the PL intensity of the sample and x, y and t coordinates, as is illustrated in figure 4.

Whilst this data cube is already useful as the intensity map can be viewed at a desired time frame, it is more beneficial to reduce the dimensionality and extract the minority charge carrier lifetime map. To do so, the cube needs to be sliced through one of the spatial dimensions rather than temporally. In other words, the intensity over time behaviour of each individual pixel for each time slice map is considered. By fitting equation (2) using least-squares fitting, the charge carrier lifetime τ is determined for the given pixel. After repeating the same process on every pixel, a charge carrier lifetime map is reconstructed for the sampled area.

2.3. Experimental setup

In addition to the simulations, an experimental setup was developed to investigate how this process can be applied in practice and what the challenges of realising this method are. The developed prototype setup is presented schematically in

Table 1. An example of a typical results matrix of the CS TRPL simulation. Each column b_i is a different TCSPC bin in the time domain, g is the bin number, and m is the number of patterns sampled. Values are counts (no units).

	b_1	b_2	b_3	⋯	b_g
Pattern 1	64 321	62 113	60 332	⋯	24
Pattern 2	63 889	61 890	58 322	⋯	32
Pattern 3	64 613	63 092	61 002	⋯	2
⋯	⋯	⋯	⋯	⋯	⋯
Pattern m	61 009	59 867	57 479	⋯	4

Table 2. Typical result file structure after running the CS TRPL reconstruction routine. Every column is the PL intensity map at bin t. The number of rows is equal to the number of pixels in the image.

	x_1	x_2	x_3	⋯	x_g
Pixel 1	6324	6212	6273	⋯	6543
Pixel 2	6123	6109	6183	⋯	6312
Pixel 3	6032	5989	6101	⋯	6211
⋯	⋯	⋯	⋯	⋯	⋯
Pixel n	2	0	1	⋯	3

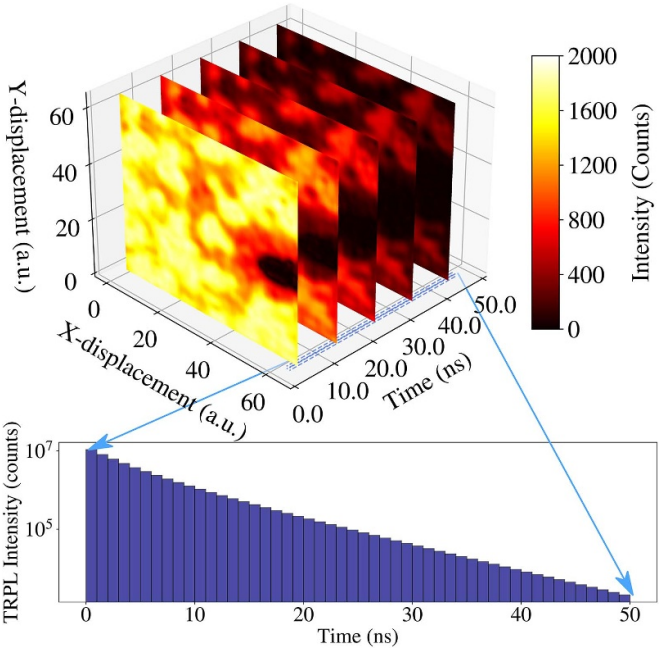

Figure 4. Data cube example of PL intensity images at varying time bins as acquired by performing CS TRPL reconstruction. Every pixel of the image consists of the estimated TRPL response.

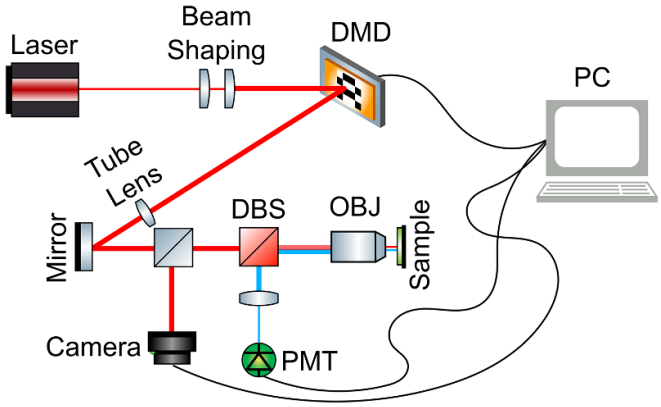

Figure 5. Schematic of the prototype system setup for TRPL Imaging. The DBS is a shortpass dichroic mirror, with 680 nm cut-off wavelength and OBJ is a microscope objective lens.

figure 5. The laser used in the setup is a Becker & Hickl 635 nm multimode diode laser. The pulse duration is dependent on the power setting and ranges from tens of ps to about 100 ps. The repetition rate can be selected from 20, 50, and 80 MHz, with average power of 8, 20, and 32 mW respectively. The pulse energy stays constant across the repetition rates. The beam is expanded and propagated onto a DMD (Vialux V-9501). The DMD consists of 1920×1080 micromirrors, each individually switchable between 2 states (on/off), allowing for any patterns to be projected onto the sample. The reflected light of the 'on' pixels of each generated pattern is focused through an Olympus MDPlan 50 × microscope objective onto the sample plane. The objective has 0.5 NA and 7.77 mm working distance. The setup gives a maximum illuminated area of 200×200 μm^2, with 1 W cm^{-2} power density. All the measurements were carried out at a temperature of approximately 20 °C within a stable lab environment. Although temperature variations can affect TRPL measurements [44], we expect that small variations (±2 °C) in temperature during measurements will have a negligible effect on measurement results.

A CMOS camera is positioned at the back focal plane of the objective to image the sample surface and it is used to achieve accurate focusing of pattern projection on the sample surface. For detecting the PL signal, a hybrid PMT module HPM-100-50 from Becker & Hickl is used. This PMT was chosen due to its high quantum efficiency at NIR wavelengths and absence of after-pulsing. A notch filter with OD6 and a 700 nm long-pass filter are used to reduce laser light leakage to the detector. Additionally, an NIR PMT from Hamamatsu was acquired with InGaAs detector to extend the range of potential samples that can be investigated. The combination of 2

detectors gives a broad range of usable wavelengths, covering 700–1700 nm spectral range.

3. Results and discussion

3.1. Simulation results

After carrying out the simulation for the measurement and reconstruction processes as described in the previous section, carrier lifetime maps were extracted. This was done by fitting an exponential decay function to the TRPL curve of each pixel. Note that for the purpose of simulation only mono-exponential decays were investigated. CS allows the use of fewer observations to reconstruct a reliable representation of a signal. In our case, this means that during the reconstruction stage, a varying sampling level can be chosen, which defines how many measured patterns are used for the reconstruction step, i.e. a sampling level of 10% means the number of patterns used in the reconstruction is equal to 10% of the number of pixels in the image. Figure 6 shows examples of the lifetime maps reconstructed at (a) 2% (b) 20% (c) 50% and (d) 99% sampling level with 64×64 px resolution. This means for the 2% case only 82 measurements were performed to acquire 4096 points of spatial information. The simulation results show that the structure is preserved and acquired even when using a low sampling level. By acquiring a larger number of measurements, the fine details of the reconstructed image become more visible. One possible application using this low sampling rate measurement is for fast initial measurements of a large area, such as a whole wafer. Non-uniform areas could be identified even when using a low sampling rate, which could then be investigated in more detail with higher resolution measurements and a higher level of sampling.

To quantify the simulation results, the structural similarity index (SSIM) [45] and mean square error (MSE) were used to compare the original virtual sample to the reconstructed images and are presented in figure 7. The SSIM ranges from 0.4 at the low sampling rate of 2%, to 0.92 at the high end. There are incremental returns in reconstructed image quality after a certain sampling rate. The SSIM reaches 0.9 at 40% sampling rate and only goes up to 0.92 at 99 %.

To further evaluate the CS TRPL process, the effect of measurement noise on reconstructed results was studied. In a physical measurement, there would be variations introduced by random measurement noise, the dark counts of the detector, resolution and dynamic range of the instruments, laser instabilities and other sources. To simulate this, we introduced small Gaussian perturbations to the counts of each bin, with the variance set as a percentage of the bin count. A Gaussian distribution of noise was adopted, as even if each source of measurement noise had a different distribution, the combination of all sources would result in a Gaussian (normal) distribution. By increasing the variance percentage, more noise is added to the virtual measurements. The measurements were then reconstructed using the same reconstruction process and algorithm, keeping the sampling level constant at 50% i.e. using 2048 measurements/patterns projected for each reconstruction.

Figure 8 shows the noisy maps reconstructed, with noise variance ranging from 0.1% to 5%. The quality of the reconstructed image rapidly deteriorates with increasing noise and at 5% the image is hardly recognisable, is highly distorted and has many pixels with failed fitting of the TRPL decays. This is an important point to consider when applying the described method experimentally. For TCSPC system to produce reliable results, sources of random noise must be minimised, such as dark counts, detector noise and laser power fluctuations. The CS part of the system is additionally highly susceptible to any signal changes over time, such as sample or laser drift. The CS methodology considers all changes in measured signal to be entirely related to spatial variations of the sample all of these must be minimised to maintain a sufficiently low level of noise. Some measurements quantifying the noise levels of the developed prototype system are described in section 3.2. These findings are crucial for the experimental implementation of a CS TRPL system, as they set the minimum noise level requirements that such system should have to provide reliable measurements.

To visualise the difference between the original values for each pixel in the virtual sample and the pixels reconstructed from noisy measurements, we can look at the correlation between them. A scatter plot where the *y*-axis presents the values of the reconstructed pixels and *x*-axis the values of the original pixels used. If the measurements were perfect and noise had no effect on reconstruction, the scatter plot would simply be a straight line with a slope of 1. This is approximated by the case in figure 9(a), where the applied noise is only 0.1%, the slope is nearly 1, and the scatter plot is very linear. Figure 9(b) has the noise level increased to 2% showing larger variance of the reconstructed lifetimes. Additionally, the slope is less than 1, i.e. the reconstructed values tend to be lower than the original ones. The above simulation results demonstrate that our approach for applying CS in TCSPC measurements is feasible. Feasibility for specific systems will depend on the noise levels, which are dependent on system parameters, such as laser power, laser uniformity and other factors.

3.2. Experimental results

From the simulation results described previously, it is clear that the sources of noise must be carefully considered when applying the method experimentally. Small deviations in the measured number of counts can lead to significant degradation in reconstruction quality.

We first consider the dark count rate of the detector and how it changes over time. To do this, the PMT shutter was closed, gain turned on, the PMT was allowed to warm up for an hour and the count rate was then monitored over 24 h. The mean dark count rate during this period was $46\,000 \pm 1000$ cps. In a TCSPC setup with the PMT shutter open and PL emission reaching the detector, the count rate is typically on the order of 10^7 cps, meaning the change in dark count rate should not have a significant effect on the measurements.

Repetition rate of 20 MHz was used throughout all the measurements carried out in this work, with laser power set to the maximum available of 8 mW average power (pulsed) at the

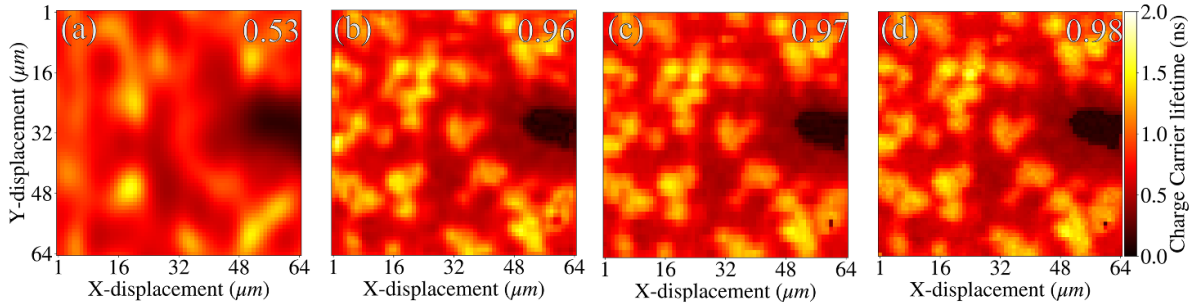

Figure 6. Reconstructed carrier lifetime maps from measuring a virtual sample in computational model. The sampling levels are 2%, 20%, 50% and 99% for the figures (a)–(d). As the sampling level is increased, more of the finer details become apparent. The numbers in white at the top right of each subfigure indicate the SSIM of the reconstructed map compared to original virtual sample.

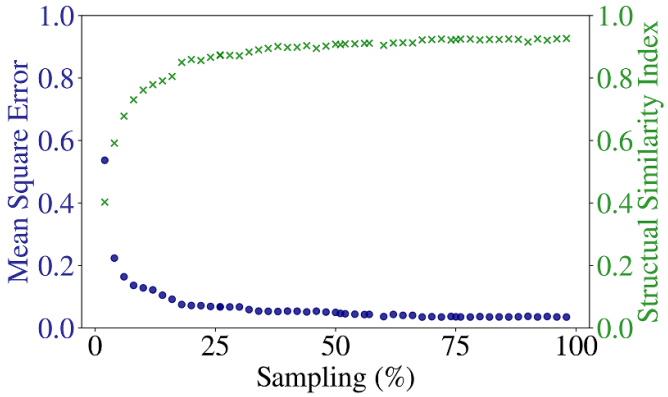

Figure 7. Green crosses show SSIM and blue circles show mean square error change with increasing sampling levels. The reconstruction quality rises rapidly at low sampling levels and levels off at around 25% sampling ratio.

laser output (before the optical system). To consider sources of noise and uncertainty in the TRPL signal for measurements with a sample, a CIGS PV device was used. To achieve this, the TRPL signal was collected 100 times from the same excitation area with 5 s collection time for each TRPL measurement. The standard deviation in the number of counts can be determined for each bin of the TRPL across the 100 measurements, as shown in figure 10. The standard deviation as a percentage of the number of counts ranged between 2% at the peak of the TRPL signal to almost 10% near the start and the end of the TRPL collection window. In the simulated results section, it was noted that standard deviation rapidly decreases the quality of the reconstructed image. At noise levels of 2% or higher, the simulated measurements were severely degraded. Regarding the experimental results, such high levels of noise affect lifetime calculations and do not allow a meaningful calculation of a lifetime value, as it is shown below.

The high noise is likely caused by several factors. To apply the pattern projection, the laser beam must be first expanded to fill the DMD area, before being focused through the objective onto the sample. The final excitation area is roughly $200 \times 200\,\mu\text{m}$, leading to a low excitation power density and decreased signal to noise ratio. Furthermore, the excitation source is a multimode laser with poor beam properties when expanded, leading to non-uniform excitation across the focused area. Finally, some sample, detector, or laser drift was observed, which also has a minor influence on the measured standard deviation. By looking at the total number of counts across each measurement, it was observed that overall detected PL intensity has a small upwards drift through the measurement duration. This is most likely caused by drift in CIGS PL efficiency [46].

A CIGS solar cell sample was chosen for use in the development of CS TRPL system. The sample exhibited strong PL signal, with emission wavelength above 1000 nm which dictated the use of a NIR PMT. An area of approximately 204 μm × 204 μm was imaged. Since this is a new method for spatial mapping, any reconstructed image must first be validated. This can either be achieved by knowing what the sample is expected to look like or by applying a known method of mapping to the same area first. Ideally, a point-by-point mapping TRPL system capable of achieving the same resolution as achieved using the CS TRPL methodology would be used. However, exciting only a single point of the sample using the DMD device (in order to achieve a direct point by point comparison with the pattern projection), severely reduces the TCSPC signal. The highest resolution point-by-point map we were able to achieve with the system was 16 px × 16 px × 12 ps. The TRPL decays were very faint, due to small excitation area and low carrier densities. Dark counts account for a high proportion of the overall measurement, making extraction of carrier lifetimes not feasible. Instead, PL maps were integrated across several time slices to reduce temporal resolution but increase the signal for each PL map. The reduced temporal resolution was 3 ns. The TRPL maps are shown in figures 11(a)–(c) for periods 0–3 ns, 3–6 ns and 6–9 ns respectively. CS TRPL measurements of the same area are expected to look the same as point-by-point scans. Therefore, these figures were compared to ones acquired using CS TRPL for validation purposed.

For testing the CS TRPL methodology, measurements and reconstructions were carried out as described in previous sections. The laser and detection parameters were kept the same as the ones used to acquire data for figure 11. Only

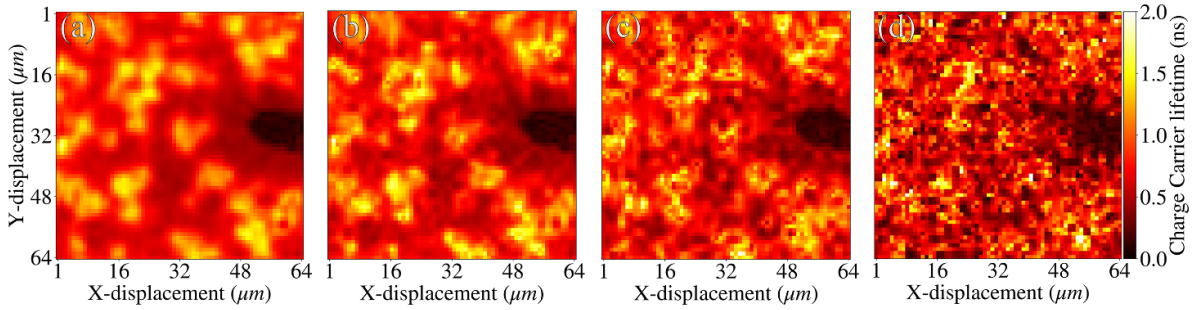

Figure 8. Carrier lifetime maps reconstructed after following the described CS TRPL methodology with Gaussian noise added to the measurements at a sampling level of 50%. The noise amplitude ranges from 0.1%, 1%, 2% to 5% for (a) to (d) respectively. The noise is added to each bin of the TRPL measurements.

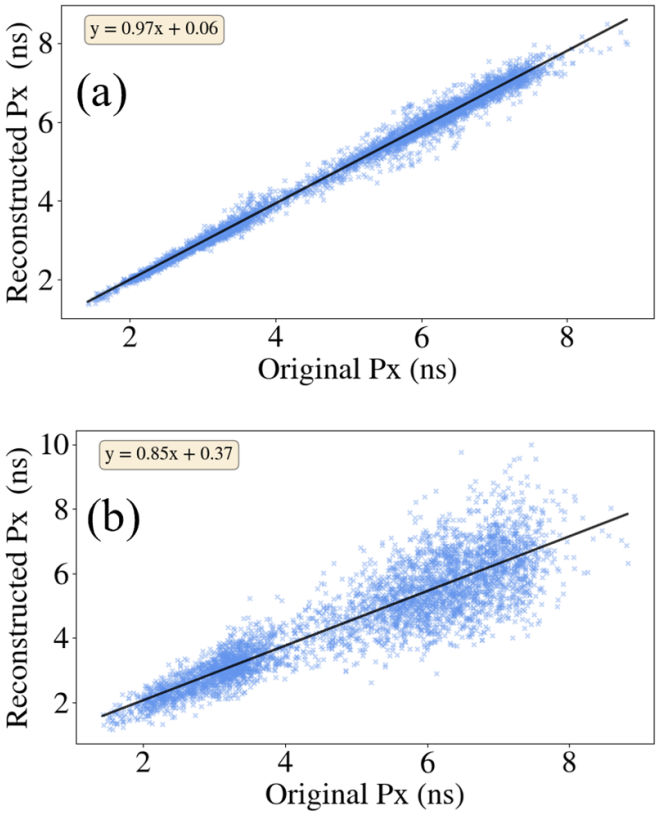

Figure 9. Scatter plots of the original lifetimes in the virtual sample vs the reconstructed lifetimes after measurements with simulated noise. (a) The noise level is 0.1%, (b) the noise level is 2%. The black line is the best fit done using the least squares method. The slope of best fit being <1 indicates that the reconstructed lifetime values tend to be lower than the original ones.

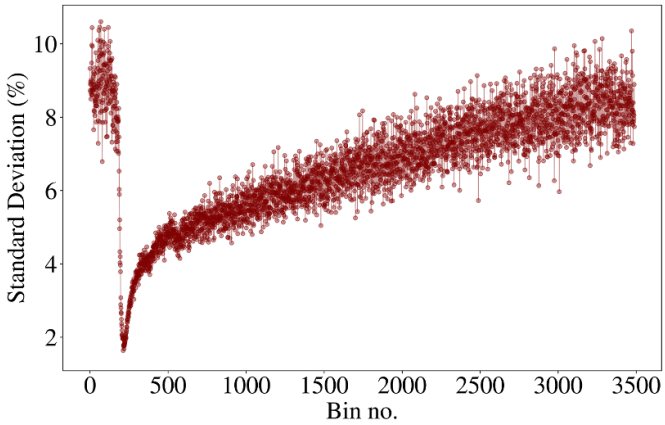

Figure 10. The standard deviation as percentage of the mean number of counts for each bin of the CIGS TRPL response. TRPL was measured 100 times from the same excitation area with collection time of 5 s for each measurement. The observed standard deviation curve is inversely proportional to the TRPL signal strength—the uncertainty is lowest at the peak of TRPL.

change was using illumination patterns instead of single-point excitation. After measurements and reconstruction, a data cube was constructed, similar to the one in figure 4, giving $16 \times 16 \times 100$ resolution ($X \times Y \times t$) with step sizes of $13\,\mu\text{m} \times 13\,\mu\text{m} \times 120$ ps. However, due to the weak signal and high noise levels it was impossible to extract a meaningful charge carrier lifetime map by fitting the exponential decay function. Instead, PL maps were integrated across several time slices to reduce temporal resolution but increase the signal for each PL map. The reduced temporal resolution was 3 ns. The TRPL maps are shown figures 12(a)–(c) for periods 0–3 ns, 3–6 ns and 6–9 ns respectively, acquired using 50% sampling level. In other words, the number of patterns measured for acquiring this image was 50% of the total number of pixels in the image. The resulting images are dominated by the features of a non-uniform laser beam used for excitation. However, a good agreement is seen between the point-by-point scan images and ones acquired using CS approach. This demonstrates the principle of the CS TRPL approach qualitatively, however, the laser source used for excitation is not suitable for quantitative validation.

The diode laser used in this experiment is typically focused to a single point, where the non-uniformities in the beam profile would not have a significant impact. However, in the case of CS, the non-uniformities in the beam profile appear in the resulting measurements.

Although it was not possible to acquire a charge carrier lifetime map with the current experimental setup, the results demonstrate the feasibility of acquiring PL maps at different time bins, allowing TRPL imaging and potentially charge carrier lifetime imaging with an upgraded system. It is also important to highlight that higher resolution CS TRPL

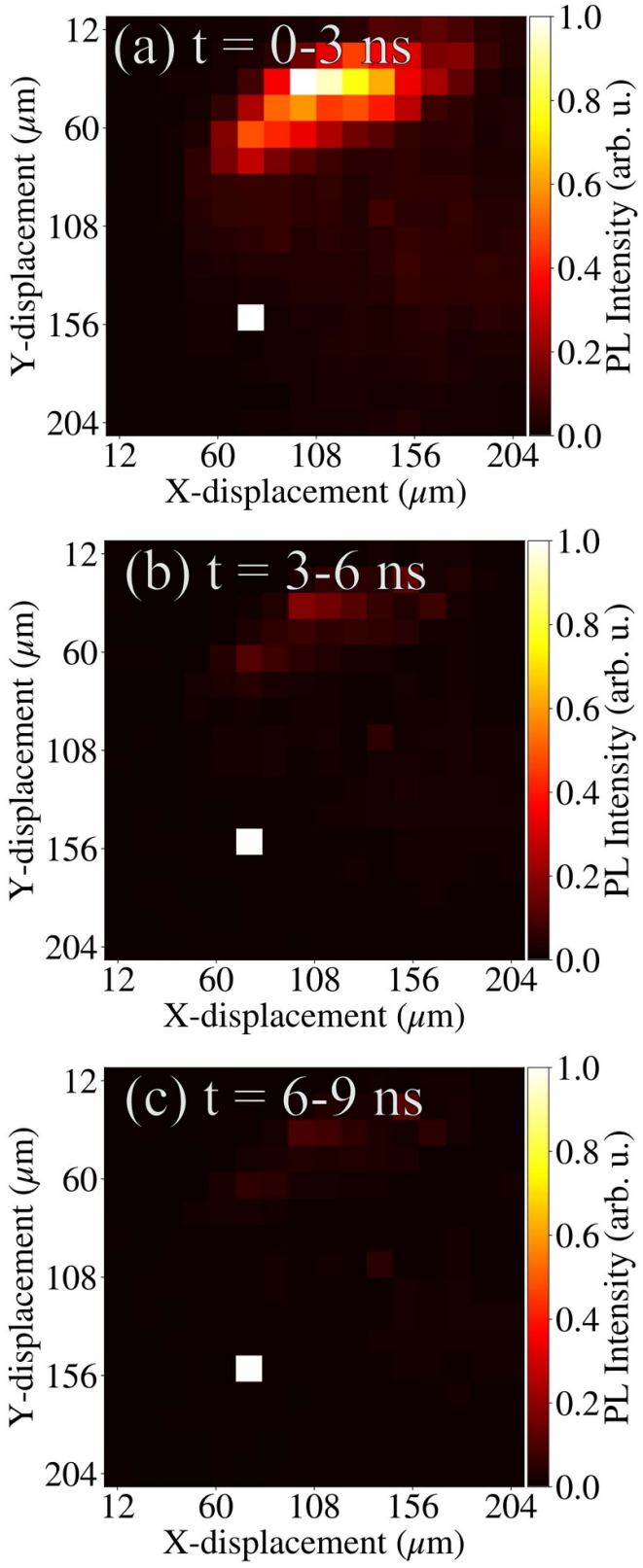

Figure 11. Normalised TRPL intensity maps of CIGS sample (a) from the peak emission to 3 ns after the peak, (b) 3–6 ns after the peak and (c). These measurements were acquired by scanning a single point across the sample using the DMD. No measurement data were acquired for the white pixel (failed decay acquisition), hence, it appears white in the maps above.

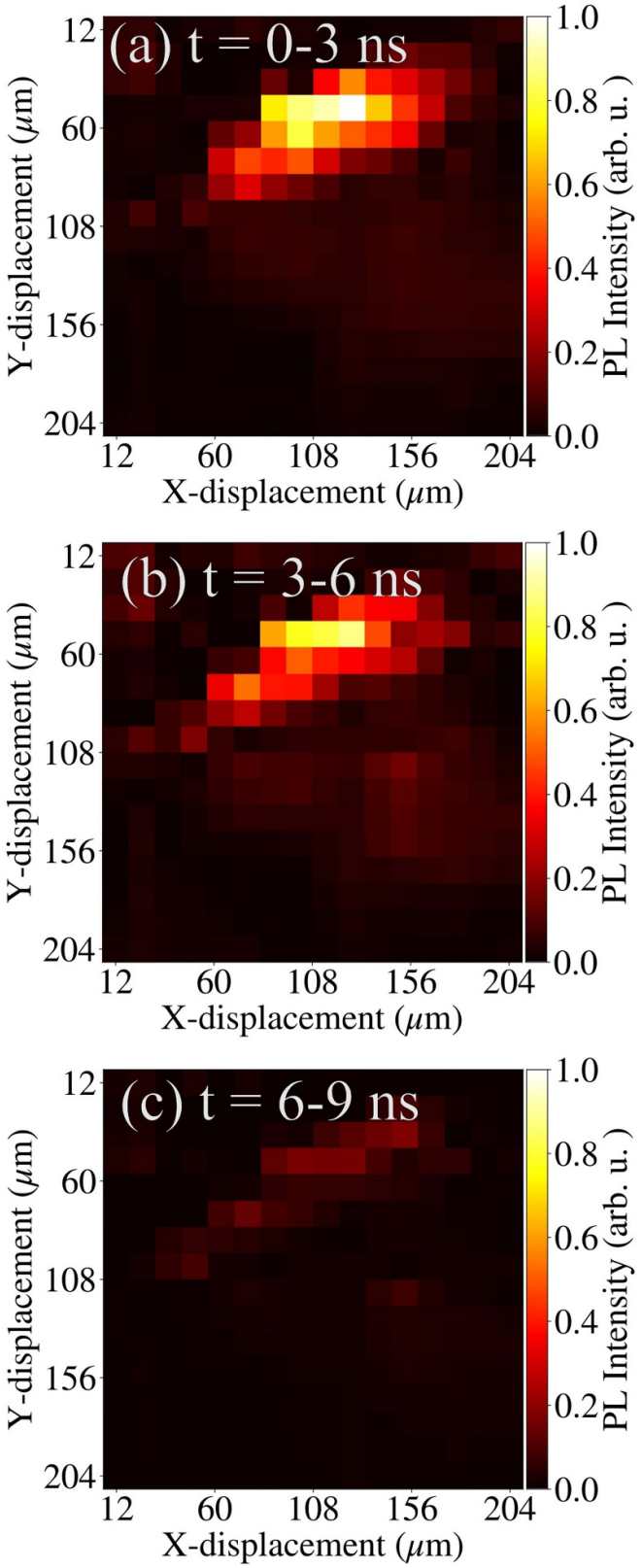

Figure 12. Normalised TRPL intensity maps of CIGS sample (a) from the peak emission to 3 ns after the peak, (b) 3–6 ns after the peak and (c) 6–9 ns reconstructed from CS TRPL methodology with 50% sampling level. The reconstructed maps show good agreement with observations in the point-by-point scan maps.

measurements were also attempted, achieving 64 px × 64 px resolutions and are provided in the supplementary material. However, the limiting factor were the point-by-point scans, as without acquiring these with the same resolution, the measurements cannot be validated.

4. Conclusions

In this work, we developed for the first time the process, methodology and an experimental approach for CS TRPL measurements using a TCSPC technique for semiconductor imaging. Initially we developed and used a computational model, for simulating DLP and TCSPC, in order to investigate the application of a CS approach. We have presented a new reconstruction process suitable for TRPL measurements, that makes use of established optimisation algorithms and achieves successful reconstruction. The feasibility of the methodology was validated, and effects of measurement noise and sampling levels were investigated through the simulations.

The sampling and reconstructing approach were then used for the development of a proof-of-concept experimental setup, based on a TCSPC system, in which a DMD has been integrated. CS TRPL results show that the method is feasible after comparing them to similar area mapped with a point-by-point scan. The simulation and initial experimental results demonstrate that this approach for CS TRPL imaging is feasible. Moreover, CS TRPL shows an improvement in the contrast of acquired maps due to exciting a broader area at the same time compared to point-by-point scan.

Through this prototype experimental system, we have determined the challenges for a CS TRPL measurement method. In the current system there is insufficient excitation power and a non-uniform laser beam profile which did not allow high quality reconstruction and the extraction of a meaningful value of charge carrier lifetime. After expanding the laser beam, the excitation density decreases significantly, reducing the amount of TRPL detectable. Furthermore, due to the highly non-uniform laser beam profile, it is challenging to determine which reconstructed sample features are real and which are only an effect of the beam profile. The noise simulations and experimental investigation showed that this technique is very sensitive to noise levels and system or sample drifts.

An upgrade of the proposed prototype system with a high-power laser with a high-quality uniform beam profile can lead to an optimised CS TRPL setup. This can offer advantages for charge carrier lifetime imaging, such as enhanced repeatability compared to scanning approaches, high image resolution and increased measurement speed. Such a system can establish the CS TRPL method a powerful technique for semiconductor characterisation and quality control. Additional sampling approaches and reconstruction algorithms dedicated to this method can also be investigated, that will benefit sampling speed and reconstruction quality.

Data availability statement

The data cannot be made publicly available upon publication because they contain commercially sensitive information. The data that support the findings of this study are available upon reasonable request from the authors.

Acknowledgments

This work was funded by the Engineering and Physical Sciences Research Council (EPSRC) iCASE studentship, Grant Number 2282139, with support from the Compound Semiconductor Centre. The work was also financially supported by the UK Government's Department for Science, Innovation and Technology (DSIT) through the National Measurement System. This project has received funding from the EMPIR programme (20IND09 'PowerElec') co-financed by the Participating States and from the European Union's Horizon 2020 research and innovation programme. The authors would also like to acknowledge James C Blakesley for the useful discussions and for providing feedback on this work.

ORCID iDs

Aidas Baltušis https://orcid.org/0000-0001-8705-7402
George Koutsourakis https://orcid.org/0000-0002-5552-1749
Sebastian Wood https://orcid.org/0000-0002-8574-0475
Stephen J Sweeney https://orcid.org/0000-0001-8561-6071

References

[1] Tanikawa T, Ohnishi K, Kanoh M, Mukai T and Matsuoka T 2018 Three-dimensional imaging of threading dislocations in GaN crystals using two-photon excitation photoluminescence *Appl. Phys. Express* **11** 31004
[2] Lee J W, Bae S H, De Marco N, Hsieh Y T, Dai Z and Yang Y 2018 The role of grain boundaries in perovskite solar cells *Mater. Today Energy* **7** 149–60
[3] Ma J, Kuciauskas D, Albin D, Bhattacharya R, Reese M, Barnes T, Li J V, Gessert T and Wei S H 2013 Dependence of the minority-carrier lifetime on the stoichiometry of CdTe using time-resolved photoluminescence and first-principles calculations *Phys. Rev. Lett.* **111** 067402
[4] Perl E E, Kuciauskas D, Simon J, Friedman D J and Steiner M A 2017 Identification of the limiting factors for high-temperature GaAs, GaInP, and AlGaInP solar cells from device and carrier lifetime analysis *J. Appl. Phys.* **122** 233102
[5] Niemeyer M, Ohlmann J, Walker A W, Kleinschmidt P, Lang R, Hannappel T, Dimroth F and Lackner D 2017 Minority carrier diffusion length, lifetime and mobility in p-type GaAs and GaInAs *J. Appl. Phys.* **122** 115702
[6] Kuciauskas D, Wernsing K, Alkaersig Jensen S, Barnes T M, Myers T H and Bartels R A 2016 Analysis of recombination

in CdTe heterostructures with time-resolved two-photon excitation microscopy *IEEE J. Photovolt.* **6** 1581–6
[7] Giudice G E, Kuksenkov D V, Temkin H and Lear K L 1999 Differential carrier lifetime in oxide-confined vertical cavity lasers obtained from electrical impedance measurements *Appl. Phys. Lett.* **74** 899–901
[8] You G, Liu J, Jiang Z, Zhu Y, Chen A, Hu Y, Xiong F, Henderson R H, Zhuang S and Xu J 2013 Time-resolved fluorescence up-conversion study of radiative recombination dynamics in III-nitride light emitting diodes over a wide bias range *Appl. Phys. Lett.* **103** 121109
[9] Lakowicz J R 2006 *Principles of Fluorescence Spectroscopy* (Spinger) pp 95–140
[10] Maiberg M and Scheer R 2014 Theoretical study of time-resolved luminescence in semiconductors. I. Decay from the steady state *J. Appl. Phys.* **116** 123710
[11] Maiberg M and Scheer R 2014 Theoretical study of time-resolved luminescence in semiconductors. II. Pulsed excitation *J. Appl. Phys.* **116** 123711
[12] Maiberg M, Hölscher T, Zahedi-Azad S and Scheer R 2015 Theoretical study of time-resolved luminescence in semiconductors. III. Trap states in the band gap *J. Appl. Phys.* **118** 105701
[13] Hall R N 1952 Electron-hole recombination in germanium *Phys. Rev.* **87** 387
[14] Shockley W and Read W T 1952 Statistics of the recombinations of holes and electrons *Phys. Rev.* **87** 835–42
[15] Candes E J and Wakin M B 2008 An introduction to compressive sampling: a sensing/sampling paradigm that goes against the common knowledge in data acquisition *IEEE Signal Process. Mag.* **25** 21–30
[16] Wang Z, Bovik A C, Sheikh H R and Simoncelli E P 2004 Image quality assessment: from error visibility to structural similarity *IEEE Trans. Image Process.* **13** 600–12
[17] Donoho D L 2006 Compressed sensing *IEEE Trans. Inf. Theory* **52** 1289–306
[18] Candes E J and Tao T 2006 Near optimal signal recovery from random projections: universal encoding strategies? *IEEE Trans. Inf. Theory* **52** 5406–25
[19] Candès E J 2008 The restricted isometry property and its implications for compressed sensing *C. R. Math.* **346** 589–92
[20] Erichson N B, Brunton S L and Kutz J N 2019 Compressed dynamic mode decomposition for background modeling *J. Real-Time Image Process.* **16** 1479–92
[21] Duarte M F, Davenport M A, Takbar D, Laska J N, Sun T, Kelly K F and Baraniuk R G 2008 Single-pixel imaging via compressive sampling: building simpler, smaller, and less-expensive digital cameras *IEEE Signal Process. Mag.* **25** 83–91
[22] Hornbeck L J 2001 The DMD^{TM} projection display chip: a MEMS-based technology *MRS Bull.* **26** 325–7
[23] Koutsourakis G, Thompson A and Blakesley J C 2021 Toward megapixel resolution compressed sensing current mapping of photovoltaic devices using digital light processing *Solar RRL* **6** 2100467
[24] Calisesi G, Ghezzi A, Ancora D, D'Andrea C, Valentini G, Farina A and Bassi A 2021 Compressed sensing in fluorescence microscopy *Prog. Biophys. Mol. Biol.* **168** 66–80
[25] Park J, Feng X, Liang R and Gao L 2020 Snapshot multidimensional photography through active optical mapping *Nat. Commun.* **11** 1–13
[26] Klein L, Touš J and Žídek K 2023 Spatially encoded hyperspectral compressive microscope for ultrabroadband VIS/NIR hyperspectral imaging *Appl. Opt.* **62** 4030
[27] Kästner B, Schmähling F, Hornemann A, Ulrich G, Hoehl A, Kruskopf M, Pierz K, Raschke M B, Wübbeler G and Elster C 2018 Compressed sensing FTIR nano-spectroscopy and nano-imaging *Opt. Express* **26** 18115–24
[28] Candès E and Romberg J 2007 Sparsity and incoherence in compressive sampling you may also like sparsity and incoherence in compressive sampling *Inverse Problems* **23** 969
[29] Baraniuk R G 2007 Compressive sensing *IEEE Signal Process. Mag.* **24** 118–21
[30] Farebrother R W 2013 *L1-Norm and L∞-Norm Estimation* (Springer)
[31] van Rossum G (The Python Development Team) 2018 The python language reference—release 3.8.1 1–160
[32] Virtanen P *et al* SciPy 1.0 Contributors 2020 {SciPy} 1.0: fundamental algorithms for scientific computing in python *Nat. Methods* **17** 261–72
[33] Hunter J D 2007 Matplotlib: a 2D graphics environment *Comput. Sci. Eng.* **9** 90–95
[34] Lam S K, Pitrou A and Seibert S Numba: a LLVM-based Python JIT Compiler (https://doi.org/10.1145/2833157.2833162)
[35] Schroder D K 2006 *Carrier Lifetimes* (Wiley) ch 7
[36] Baraniuk R, Davenport M, DeVore R and Wakin M 2008 A simple proof of the restricted isometry property for random matrices *Constr. Approx.* **28** 253–63
[37] Blasiok J, Lopatto P, Luh K, Marcinek J and Rao S 2019 An improved lower bound for sparse reconstruction from subsampled Hadamard matrices *Proc.—Annual IEEE Symp. on Foundations of Computer Science, FOCS* vol 2019 pp 1564–7
[38] Zhang Z, Wang X, Zheng G and Zhong J 2017 Hadamard single-pixel imaging versus Fourier single-pixel imaging *Opt. Express* **25** 19619–39
[39] Becker W 2021 *The Bh TCSPC Handbook* (Becker & Hickl GmbH) (available at: https://www.becker-hickl.com/literature/documents/flim/the-bh-tcspc-handbook/)
[40] Salthammer T 1992 Numerical simulation of pile-up distorted time-correlated single photon counting (TCSPC) data *J. Fluorescence* **2** 23–27
[41] van den Berg E and Friedlander M P 2020 SPGL1: a solver for large-scale sparse reconstruction
[42] Doll A, Ravasi M and Relyea D 2020 {SPGL1} Python implementation
[43] van den Berg E and Friedlander M P 2008 Probing the Pareto frontier for basis pursuit solutions *SIAM J. Sci. Comput.* **31** 890–912
[44] Weiss T P, Carron R, Wolter M H, Löckinger J, Avancini E, Siebentritt S, Buecheler S and Tiwari A N 2019 Time-resolved photoluminescence on double graded Cu(In,Ga)Se_2–Impact of front surface recombination and its temperature dependence *Sci. Technol. Adv. Mater.* **20** 313–23
[45] Wang Z and Li Q 2011 Information content weighting for perceptual image quality assessment *IEEE Trans. Image Process.* **20** 1185–98
[46] Kenny R P, Chatzipanagi A I and Sample T 2014 Preconditioning of thin-film PV module technologies for calibration *Prog. Photovol. Res. Appl.* **22** 166–72